

Dislocation-mediated ultrahigh mechanical properties in nano-TiN

Jie Zhou^{1,2}, Fang Peng,^{1,*} Fang Hong,^{3,4,5,†} and Binbin Yue^{2,‡}

¹*Institute of Atomic and Molecular Physics, Sichuan University, Chengdu 610065, China*

²*Center for High Pressure Science and Technology Advanced Research, 10 East Xibeiwang Road, Haidian, Beijing 100193, China*

³*Beijing National Laboratory for Condensed Matter Physics, Institute of Physics, Chinese Academy of Sciences, Beijing 100190, China*

⁴*School of Physical Sciences, University of Chinese Academy of Sciences, Beijing 100190, China*

⁵*Songshan Lake Materials Laboratory, Dongguan, Guangdong 523808, China*



(Received 2 January 2024; accepted 6 March 2024; published 26 March 2024)

Stiffness and ductility can be achieved by reducing the grain size of ceramics to the nanometer scale. However, the deformation mechanism of nanoceramics is still controversial due to technical limitations. In this paper, via synchrotron radial x-ray diffraction technology combined with a diamond anvil cell, the deformation behavior of nanosized titanium nitride (TiN) has been studied *in situ* under high-pressure conditions up to 41.3 GPa. Results show that the nano-TiN exhibits a much higher bulk modulus and yield strength than its bulk counterpart. Nano-TiN starts to yield at around 17.3 GPa and the maximum yield strength is approximately 8.7 GPa at 41.3 GPa. The presence of 110 and 001 texture in nanosized TiN was confirmed under pressure, indicating a strong activity of dislocation. This paper suggests that the reduction in grain size to the nanoscale improves both the stiffness and ductility of TiN via a dislocation-mediated mechanism.

DOI: [10.1103/PhysRevMaterials.8.036001](https://doi.org/10.1103/PhysRevMaterials.8.036001)

I. INTRODUCTION

Ceramic materials have the advantages of high hardness, wear resistance, corrosion resistance, etc., and are widely used in daily life. The high atomic bonding strength and ordered crystal structure lead to the excellent hardness and stiffness of ceramics and enable them to resist scratches [1]. Ceramics with high hardness tend to be more resistant to wear [2]. Their high stiffness makes them less prone to elastic deformation under stress. Additionally, the chemical stability and dense structure of ceramics contribute to their resistance to corrosion [3]. However, compared to metals, ceramics generally lack ductility due to their inherent resistance to plastic deformation [4–7]. To solve this problem, previous researchers have proposed solutions such as microstructure regulation, coating technology, and heat treatment [8–10]. Most importantly, nanocrystals have contributed to the ductility of ceramics in the past few decades [4,5,11,12]. Furthermore, nanoceramics also show excellent performance in the fields of catalysis, sensing, energy storage, and biomedical applications [13–16].

Based on Cottrell's classical concept, below a critical grain size, the stress required to nucleate a crack is less than the stress required to propagate the crack, and ductility can be expected in nanoceramics [17]. However, the main mechanism of ductility in nanoceramics is still unclear. Many researchers have proposed that brittle ceramics, which lack sufficient dislocation activity, may exhibit better ductility in the nanometer range due to greatly increased

diffusivities. For example, observations of the deformation process in CaF_2 and TiO_2 suggest that ductility originates from the diffusional flow of atoms along the intergranular interfaces [4,5,18]. In the meantime, some researchers have suggested that the dislocation-mediated deformation is effective in nanoceramics. The observations of stiffness and texture in nano- MgAl_2O_4 indicate that dislocations can make nanoceramics both stiff and ductile [19]. Surface dislocation nucleation in nano- MgO has also been investigated using a multistep modeling approach [20]. Therefore, further investigation is still needed to deepen our understanding of the deformation mechanism (both elastic and plastic deformation) of nanoceramics and its differences from bulk ceramics.

In this paper, nano-TiN was used to study the deformation of nanoceramics under extreme compression. TiN has a cubic structure and remains stable over a wide pressure range, which allows us to focus on pressure-induced deformation mechanisms [21,22]. As a ceramic material with the advantages of high melting point, high hardness, high wear resistance, and high corrosion resistance [23–25], the mechanical properties of micron-sized TiN have been extensively studied [22,26,27]. Wang *et al.* also explored the size-dependent high-pressure behavior of nanocrystalline TiN and found that nano-TiN had better compression resistance than micron-TiN [21]. However, the deformation behavior of nano-TiN is still unclear. In order to explore the deformation behavior of nanoceramics under high pressure, radial x-ray diffraction in a diamond anvil cell (rDAC-XRD) was conducted on 15-nm TiN. Our paper shows that nano-TiN has a larger bulk modulus and higher yield strength compared to bulk TiN. Additionally, the observation of 110 and 001 texture in nano-TiN suggests a dislocation-mediated stiff and ductile behavior under high pressure.

*pengfang@scu.edu.cn

†hongfang@iphy.ac.cn

‡yuebb@hpstar.ac.cn

II. EXPERIMENT PROCEDURE

The high-pressure radial x-ray diffraction experiments were conducted at the BL04 beamline of the ALBA synchrotron in Spain. The experiments were performed at room temperature. To generate the high-pressure conditions and allow radial diffraction, a panoramic diamond anvil cell with a large side opening was used. Boron epoxy inserted into a Kapton ring was used as the x-ray transparent gasket. The sample used in the experiment was nanoscale TiN powder with an average particle size of approximately 15 nm. The nano-TiN powder was loaded into a 50- μm -diameter sample hole. To monitor the applied pressure, a platinum foil with a thickness of approximately 10 μm was also loaded into the sample hole as a pressure marker [28].

No pressure transmitting medium was used in the experiments to achieve a uniaxial compression on the sample. A monochromatic x-ray beam with a wavelength of 0.4246 \AA was used in the experiments. The x-ray beam was focused onto the sample with a size of $15 \times 15 \mu\text{m}^2$. Prior to the experiment, instrument parameters such as the sample-to-detector distance, beam center, and detector tilt were calibrated using a LaB₆ standard. Diffraction patterns were collected for both platinum and TiN. For platinum, diffraction lines (111), (200), and (220) were used to determine the pressure. For TiN, diffraction lines of (111), (200), (220), (311), and (222) were detected. Quantitative analysis of the diffraction data was performed using the MAUD [29,30] (Materials Analysis Using Diffraction) software. In the analysis of the experimental data, various information was extracted, including lattice parameters, texture (lattice preferred orientation), grain size, stress, and microstrain.

In a rDAC-XRD experiment, uniaxial stress is applied to the sample along the axial loading direction, which is the direction perpendicular to the culets of diamond anvils. This direction experiences the maximum stress σ_3 . Radial directions are parallel to the culets of the diamond anvils, experiencing the minimum stress σ_1 . The difference between the maximum and minimum stress is known as the differential stress, denoted as t . This differential stress represents the stress experienced by the sample during the high-pressure experiment and Eq. (1) can be written as [31]

$$t = \sigma_3 - \sigma_1. \quad (1)$$

Based on the lattice strain theory [32,33], the measured interplanar spacing $d_m(hkl)$ of a polycrystalline sample in rDAC-XRD experiments is a function of the angle Ψ between the loading direction of the diamond anvil and the normal direction of the diffraction plane:

$$d_m(hkl) = d_p(hkl)[1 + (1 - 3 \cos^2 \Psi)Q(hkl)], \quad (2)$$

where $d_m(hkl)$ is the measured d spacing, $d_p(hkl)$ is the d spacing under the hydrostatic pressure, and $Q(hkl)$ represents the corresponding lattice strain [31–33]. The relationship between the differential stress t and $Q(hkl)$ is given by Eq. (3) [32,33]:

$$Q(hkl) = t/(6G), \quad (3)$$

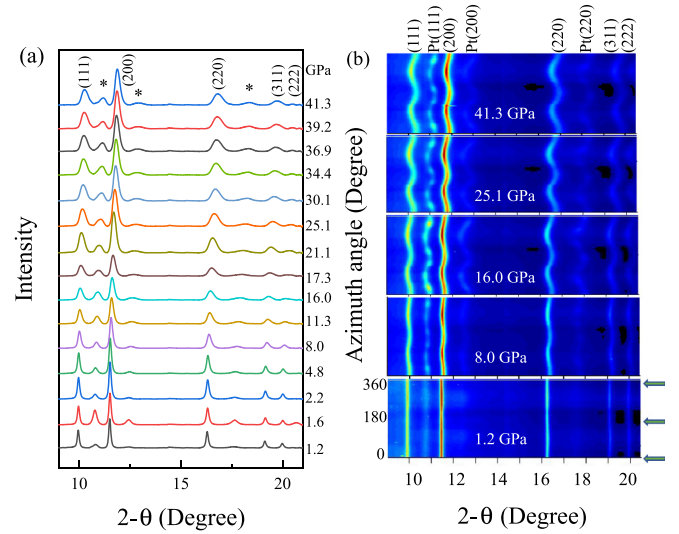


FIG. 1. X-ray diffraction patterns of the nano-TiN sample under pressure up to 41.3 GPa at room temperature. (a) Integrated x-ray diffraction patterns upon compression. Black stars indicate diffraction peaks from Pt. (b) Selected unrolled diffraction patterns. Green arrows at the right side indicate the compression direction.

where G represents the shear modulus of the polycrystalline material. The shear modulus G measures the material's resistance to shear deformation.

III. RESULTS AND DISCUSSIONS

The collected two-dimensional diffraction images were processed by the software DIOPTAS [34] to obtain the integrated diffraction patterns. During the measurement, 15-nm TiN was compressed to 41.3 GPa at room temperature (Fig. 1). No new diffraction lines were observed up to the highest pressure, indicating no phase transition in this pressure range. This is consistent with previous studies that nano-TiN and micron-TiN are both stable up to ≈ 45 GPa [21,22], suggesting that the reduction of grain size to the nanoscale does not cause any phase transitions within the investigated pressure range.

Selected unrolled diffraction patterns are presented in Fig. 1(b). The curvature of the diffraction lines can provide insight into how lattice strain develops in response to applied differential stress. At a pressure of 1.2 GPa, the diffraction lines exhibit little to no curvature, indicating minimal lattice strain and stress on the nano-TiN samples. As pressure increases, all diffraction lines shift to a higher two-theta angle. Curvature also starts to show and becomes more obvious under higher pressure, indicating an increase of lattice strain. The variation in intensity with azimuthal angle on each diffraction line indicates the lattice preferred orientation or texture of the crystal. With further compression, the texture gradually becomes pronounced.

Diffraction images were imported to MAUD software to get quantitative analysis by Rietveld refinement. Figures 2(a) and 2(b) represent the lattice parameters and unit-cell volume as a function of pressure for nano-TiN. The relationship between pressure and volume for nano-TiN was fitted using the

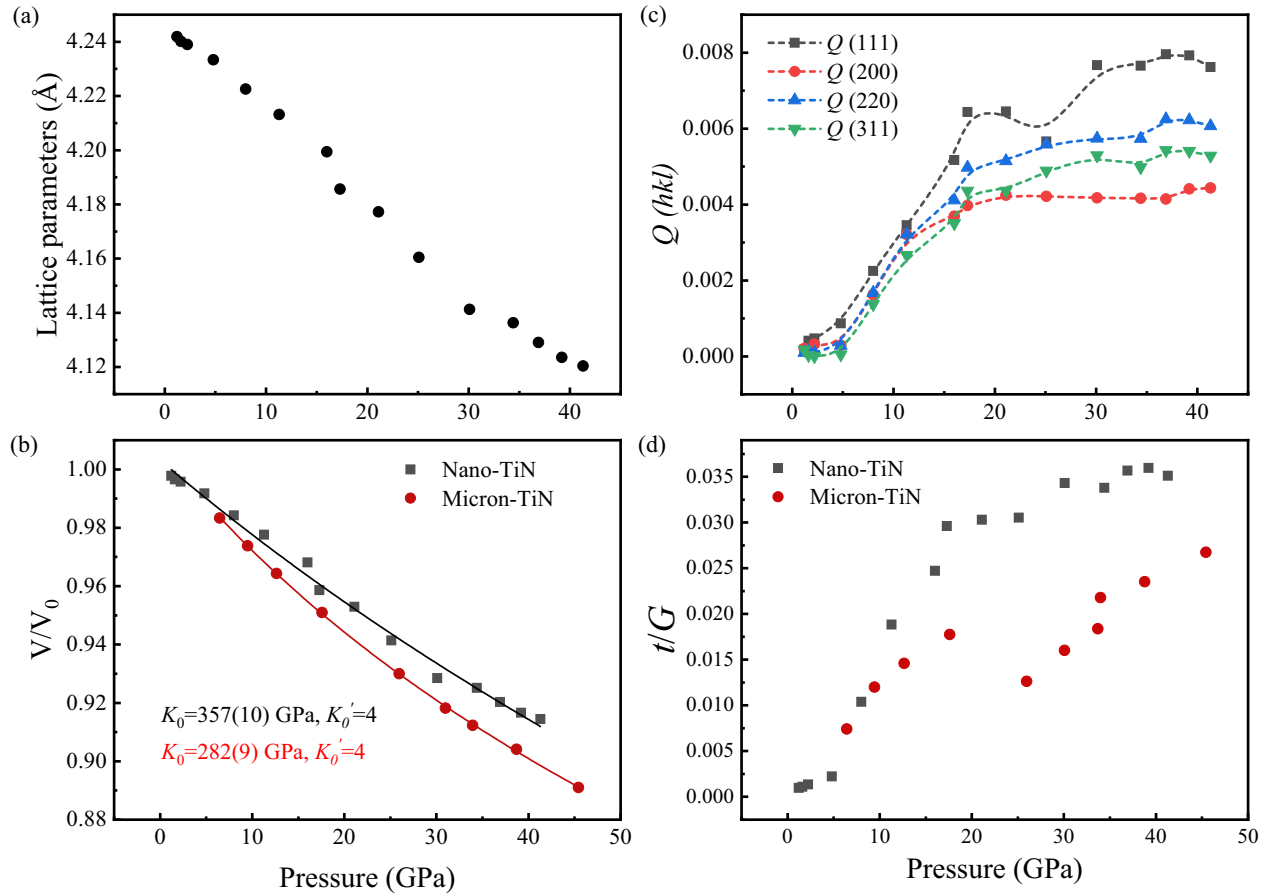


FIG. 2. Refinement results of nano-TiN under high pressure: (a) lattice parameters, (b) variations of relative unit-cell volume compared with micron-TiN [22], (c) lattice strain, and (d) the average t/G compared with micron-TiN [22]. Solid lines in (b) are equation of state fitting results. The dotted lines in (c) are guides to the eyes.

Birch-Murnaghan equation of state. The fitting results yield a bulk modulus K_0 of 357 ± 10 GPa, with a fixed K'_0 (the pressure derivative of the bulk modulus) of 4. This value is comparable to or slightly higher than the bulk modulus of nano-TiN obtained under hydrostatic compression [21]. This is due to the fact that the nonhydrostatic compression usually leads to an overestimation of bulk modulus, as observed in other materials [35,36]. Previously, rDAC-XRD was conducted on micron-TiN by Chen *et al.* [22], and its volume as a function of pressure has also been plotted in Fig. 2(b). It is found that nano-TiN has a higher bulk modulus than micron-TiN ($K_0 = 282 \pm 9$ GPa with K'_0 fixed at 4). In comparison with the relevant nitrides, it was noted that the K of this nano-TiN was also higher than that of c -BC₂N and γ -Si₃N₄ [37,38].

By analyzing the slope of $d_m(hkl)$ vs $1-3\cos^2\Psi$ based on Eq. (2), we can obtain the $Q(hkl)$ for different diffraction planes [Fig. 2(c)]. All $Q(hkl)$ values increase rapidly during the initial compression. Beyond 17.3 GPa, the $Q(111)$, $Q(220)$, and $Q(311)$ continue to increase slowly, while $Q(200)$ is almost stable. $Q(111)$ reaches the largest value of 0.008, while $Q(200)$ finally stabilizes at the smallest value with 0.004 at 41.3 GPa. It reveals that the maximum stress is suffered on the (111) plane, and the minimum stress is undergone on the (200) plane. The different behavior of these lattice strains

reveals significant anisotropy under pressure. After further analysis, the average t/G of nano-TiN under high pressure was calculated and compared with that of micron-TiN [22], as shown in Fig. 2(d). The t/G values of both nano-TiN and micron-TiN increase fast below ≈ 17 GPa and then enter into a plateau, indicating the beginning of yielding. At the highest pressure, t/G values reach 0.035 and 0.027 for nano-TiN and micron-TiN, respectively. The higher t/G of nano-TiN suggests that reducing the grain size from microscale to nanoscale effectively enhances the stiffness of TiN.

The elastic modulus of nano-TiN has also been obtained and is plotted in Fig. 3(a). The high-pressure bulk modulus (K) of nano-TiN was obtained using the Birch-Murnaghan equation. We used the approximate K/G ratio of 1.926 ± 0.37 for ceramics to calculate the shear modulus of TiN under pressure [39]. This result gives a G value of 195.4 ± 34 GPa at ambient conditions, which is similar to both the theoretical value of 190 GPa and the experimental bulk modulus of 189 GPa for nano-TiN [40,41]. Finally, Young's modulus (E) can be calculated using the formula $E = 9KG/(3K + G)$.

With the high-pressure shear modulus, the differential stress of this nano-TiN under high pressure was calculated, and the results are shown in Fig. 3(b). It is clear that t increases rapidly below 17.3 GPa, and then it enters into a plateau with a highest value of ≈ 8.7 GPa. In the work of Chen

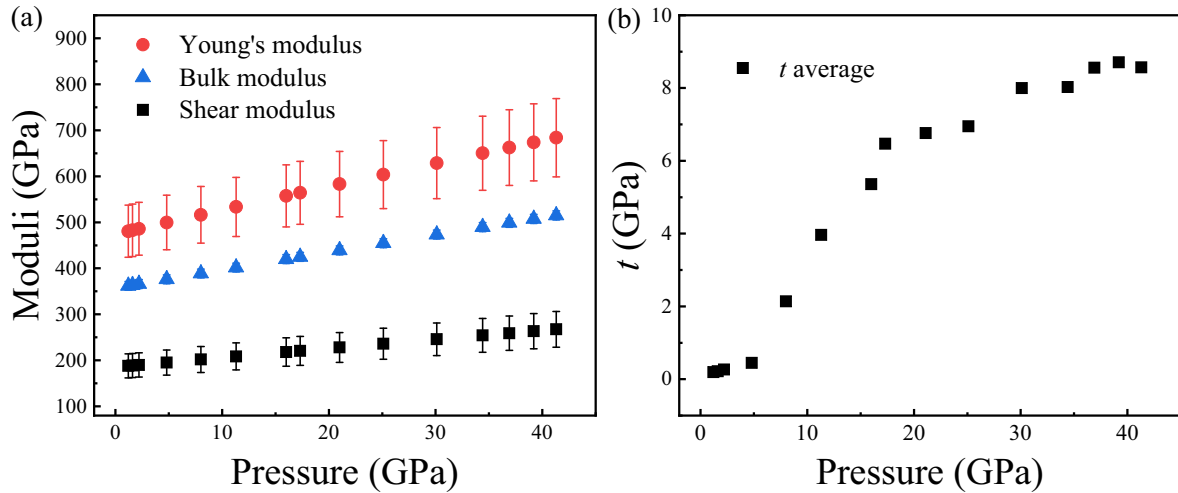


FIG. 3. (a) The moduli values of the nano-TiN sample and (b) differential stress of this nano-TiN as a function of pressure.

et al., the differential stress t of micron-TiN was calculated to be 8.6 GPa at 45.4 GPa with a much lower K/G ratio of 1.37 [22]. By comparing previous theoretical calculations and other experimental articles, it is more reasonable to calculate the G value using a K/G of 1.926 [26,27,39]. The t value of micron-TiN at 45.4 GPa was recalculated to be ≈ 6.1 GPa using the K/G of 1.926, which is much lower than that of nano-TiN. The maximum uniaxial stress supported by a material is defined by the yield strength, and t represents the lower end of the material's yield strength under pressure [42]. Therefore, nano-TiN exhibits a higher yield strength, indicating superior stiffness compared to micron-TiN.

As mentioned above, texture can be observed for nano-TiN under high pressure. Throughout the analysis, the texture information was obtained by imposing axial symmetry about the compression direction and represented in the inverse pole figure (IPF) (Fig. 4). Texture is shown with a maximum at 110 in the IPF, indicating that the 110 plane is oriented perpendicular to the compression direction. Another weaker maximum appears at 001. The 110 texture and 001 texture persist up to 41.3 GPa. This result indicates that dislocation-mediated plastic deformation is active in the nano-TiN. Density of dislocations in nano-TiN increases with pressure and causes hardening which leads to an increase of the yield stress.

The texture and slip systems in crystals with the NaCl crystal structure under high pressure have been proposed by many

researchers. Via elasto-visco plastic self consistent modeling, Lin *et al.* found that a dominant $\{100\}\langle 011 \rangle$ slip system in MgO would cause a 110 texture together with a largest $Q(200)$ and a lowest $Q(111)$, while a dominant $\{110\}\langle 1-10 \rangle$ slip induced a 001 texture with a largest $Q(111)$ and a lowest $Q(200)$ [43]. For (Mg,Co,Ni,Cu,Zn)O, a dominant $\{100\}\langle 011 \rangle$ slip system was proposed at the initial compression, and then the activity of slip system $\{110\}\langle 1-10 \rangle$ increases and finally becomes dominant under higher pressure. The activation of both slip systems induces two maxima in the IPF (100 and 110) [44]. Furthermore, a dominant $\{110\}\langle 1-10 \rangle$ slip system in ferropicrlase [(Mg_{0.83}, Fe_{0.17})O] would cause a 001 texture [45]. For nano-TiN, the largest $Q(111)$ and the lowest $Q(200)$ in the high-pressure range suggest the large contribution of the $\{110\}\langle 1-10 \rangle$ slip system. The $\{100\}\langle 011 \rangle$ slip system also contributes, as evidenced by the presence of the 110 texture in the IPFs.

IV. CONCLUSIONS

In summary, we systematically investigated the deformation behavior of nano-TiN under high pressure via rDAC-XRD technique. The results show that nano-TiN has a larger bulk modulus and higher yield strength than micron-TiN. It was also found that nano-TiN has 110 and 001 texture with the contribution of two potential slip systems $\{110\}\langle 0-10 \rangle$ and $\{100\}\langle 011 \rangle$. These results demonstrate that

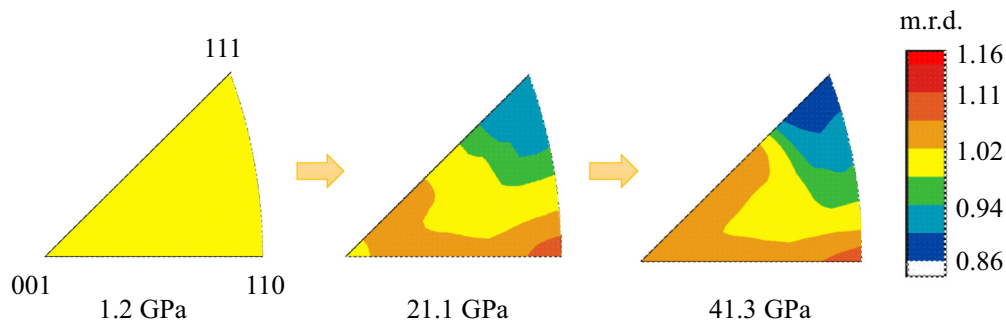


FIG. 4. Texture evolution of nano-TiN under high pressure. Pole densities are measured in multiples of random distribution (m.r.d.).

dislocation-mediated deformation mechanisms are operative in stressed nano-TiN. Our study of nano-TiN provides evidence that dislocations contribute to the stiffness and ductility of nanoceramics. This knowledge contributes to a broader understanding of the mechanics of nanomaterials, guiding future material design and applications in different fields.

ACKNOWLEDGMENTS

The authors acknowledge the support of National Natural Science Foundation of China (Grants No. 12004014, No. 12374050, No. 22090041, No. U1930401, and No. 12074273). The synchrotron radiation experiments were performed at MSPD beamline at ALBA Synchrotron.

-
- [1] B. Gilbert, F. Huang, H. Zhang, G. A. Waychunas, and J. F. Banfield, *Science* **305**, 651 (2004).
- [2] E. Medvedovski, *Wear* **249**, 821 (2001).
- [3] K. Wang, J. Unger, J. D. Torrey, B. D. Flinn, and R. K. Bordia, *J. Eur. Ceram. Soc.* **34**, 3597 (2014).
- [4] A. Domínguez-Rodríguez, D. Gómez-García, E. Zapata-Solvas, J. Z. Shen, and R. Chaim, *Scr. Mater.* **56**, 89 (2007).
- [5] J. Karch, R. Birringer, and H. Gleiter, *Nature (London)* **330**, 556 (1987).
- [6] W. Zhai, L. Bai, R. Zhou, X. Fan, G. Kang, Y. Liu, and K. Zhou, *Adv. Sci.* **8**, 2003739 (2021).
- [7] K. L. Arun, M. Udhayakumar, and N. Radhika, *J. Bio. Tribo. Corros.* **9**, 11 (2023).
- [8] B. R. Lawn, N. P. Padture, H. Cait, and F. Guiberteau, *Science* **263**, 1114 (1994).
- [9] Y. X. Wang and S. Zhang, *Surf. Coatings Technol.* **258**, 1 (2014).
- [10] Y. Waku, N. Nakagawa, T. Wakamoto, H. Ohtsubo, K. Shimizu, and Y. Kohtoku, *Nature (London)* **389**, 49 (1997).
- [11] W. J. Clegg, *Science* **286**, 1097 (1999).
- [12] D. Jang and J. R. Greer, *Nat. Mater.* **9**, 215 (2010).
- [13] S. Mitchell, R. Qin, N. Zheng, and J. Pérez-Ramírez, *Nat. Nanotechnol.* **16**, 129 (2021).
- [14] U. Shashikumar, B. Chandra Jha, S. Chawla, C. Mustansar Hussain, G. Andaluri, Y. C. Lin, and V. K. Ponnusamy, *Fuel* **336**, 126829 (2023).
- [15] A. J. T. Naik, R. Gruar, C. J. Tighe, I. P. Parkin, J. A. Darr, and R. Binions, *Sensors and Actuators B: Chemical* **217**, 136 (2014).
- [16] Y. Hong, H. Fan, B. Li, B. Guo, M. Liu, and X. Zhang, *Mater. Sci. Eng. R* **70**, 225 (2010).
- [17] A. Kochendörfer, H. D. Schulze, and H. Riedel, *Int. J. Fract.* **11**, 365 (1975).
- [18] H. Gleiter, *Prog. Mater. Sci.* **33**, 223 (1990).
- [19] B. Chen, Y. Huang, J. Xu, X. Zhou, Z. Chen, H. Zhang, J. Zhang, J. Qi, T. Lu, J. F. Banfield, J. Yan, S. V. Raju, A. E. Gleason, S. Clark, and A. A. MacDowell, *J. Mater. Res.* **34**, 1489 (2019).
- [20] J. Amodeo, E. Maras, and D. Rodney, *Npj Comput. Mater.* **7**, 60 (2021).
- [21] Q. Wang, D. He, F. Peng, L. Xiong, J. Wang, P. Wang, C. Xu, and J. Liu, *Solid State Commun.* **182**, 26 (2014).
- [22] H. Chen, F. Peng, H. K. Mao, G. Shen, H. P. Liermann, Z. Li, and J. Shu, *J. Appl. Phys.* **107**, 113503 (2010).
- [23] J. B. Price, J. O. Borland, and S. Selbrede, *Thin. Solid. Films* **236**, 311 (1993).
- [24] J. P. Tu, *Corros. Sci.* **42**, 147 (2000).
- [25] H. Kuwahara, N. Mazaki, M. Takahashi, T. Watanabe, X. Yang, and T. Aizawa, *Mater. Sci. Eng. A* **319**, 687 (2001).
- [26] K. Prasert, P. Thanomngam, and K. Sarasamak, *Adv. Mater. Res.* **802**, 109 (2013).
- [27] K. Liu, X. Zhou, H. Chen, and L. Lu, *Physica B: Condens. Matter* **407**, 3617 (2012).
- [28] N. C. Holmes, J. A. Moriarty, G. R. Gathers, and W. J. Nellis, *J. Appl. Phys.* **66**, 2962 (1989).
- [29] L. Lutterotti, S. Matthies, H. R. Wenk, A. S. Schultz, and J. W. Richardson, *J. Appl. Phys.* **81**, 594 (1997).
- [30] H. M. Rietveld, *J. Appl. Crystallogr.* **2**, 65 (1969).
- [31] S. Merkel, H. R. Wenk, J. Shu, G. Shen, P. Gillet, H. Mao, and R. J. Hemley, *J. Geophys. Res. Solid Earth* **107**, ECV 3 (2002).
- [32] A. K. Singh, H. K. Mao, J. Shu, and R. J. Hemley, *Phys. Rev. Lett.* **80**, 2157 (1998).
- [33] A. K. Singh, C. Balasingh, H. K. Mao, R. J. Hemley, and J. Shu, *J. Appl. Phys.* **83**, 7567 (1998).
- [34] C. Prescher and V. B. Prakapenka, *High Press. Res.* **35**, 223 (2015).
- [35] O. Gomis, J. A. Sans, R. Lacomba-Perales, D. Errandonea, Y. Meng, J. C. Chervin, and A. Polian, *Phys. Rev. B* **86**, 054121 (2012).
- [36] B. Yue, F. Hong, S. Merkel, D. Tan, J. Yan, B. Chen, and H. K. Mao, *Phys. Rev. Lett.* **117**, 135701 (2016).
- [37] B. Kiefer, S. R. Shieh, T. S. Duffy, and T. Sekine, *Phys. Rev. B* **72**, 014102 (2005).
- [38] H. Dong, D. He, T. S. Duffy, and Y. Zhao, *Phys. Rev. B* **79**, 014105 (2009).
- [39] K. K. Phani and D. Sanyal, *Mater. Sci. Eng. A* **490**, 305 (2008).
- [40] M. S. El-Eskandarany, *J. Mater. Eng. Perform.* **26**, 2954 (2017).
- [41] I. V. Safronov, V. I. Shymanski, V. V. Uglov, N. T. Kvasov, and N. N. Dorozhkin, *Comput. Mater. Sci.* **123**, 256 (2016).
- [42] D. He and T. S. Duffy, *Phys. Rev. B* **73**, 134106 (2006).
- [43] F. Lin, S. Couper, M. Jugle, and L. Miyagi, *Minerals* **9**, 650 (2019).
- [44] B. Yue, W. Dai, X. Zhang, H. Zhang, W. Zhong, B. Liu, S. Kawaguchi, and F. Hong, *Scr. Mater.* **219**, 114879 (2022).
- [45] J. F. Lin, H. R. Wenk, M. Voltolini, S. Speziale, J. Shu, and T. S. Duffy, *Phys. Chem. Miner.* **36**, 585 (2009).